Thermal Contributions to the Local and Long-Range Structural Disorder in $CH_3NH_3PbBr_3$

Nicholas J. Weadock,[1,2,*] Cameron MacKeen,[3] Xixi Qin,[4,5] Louis Waquier,[6] Yevgeny Rakita,[7] Julian A. Vigil,[8,9] Hemamala I. Karunadasa,[9,10] Volker Blum,[4,11] Michael F. Toney,[1,2,12] and Frank Bridges[3]

[1] *Materials Science and Engineering, University of Colorado, Boulder, Boulder, Colorado 80309, USA*

[2] *Department of Chemical and Biological Engineering, University of Colorado, Boulder, Boulder, Colorado 80309, USA*

[3] *Physics Department, University of California, Santa Cruz, California 95064, USA*

[4] *Thomas Lord Department of Mechanical Engineering and Materials Science, Duke University, Durham, North Carolina 27708, USA*

[5] *Duke University Program in Materials Science and Engineering, Duke University, Durham, North Carolina 27708, USA*

[6] *SSRL Materials Science Division, SLAC National Accelerator Laboratory, Menlo Park, California 94025, USA*

[7] *Department of Materials Engineering, Ben-Gurion University of the Negev, Beer-Sheva 84105, Israel*

[8] *Department of Chemical Engineering, Stanford University, Stanford, California 94305, USA*

[9] *Department of Chemistry, Stanford University, Stanford, California 94305, USA*

[10] *Stanford Institute for Materials and Energy Sciences, SLAC National Accelerator Laboratory, Menlo Park, California 94025, USA*

[11] *Department of Chemistry, Duke University, Durham, North Carolina 27708, USA*

[12] *Renewable and Sustainable Energy Institute (RASEI), University of Colorado, Boulder, Boulder, Colorado 80309, USA*

(Received 7 September 2022; revised 20 April 2023; accepted 7 June 2023; published 21 July 2023)

The hybrid lead halide perovskite (LHP) family exhibits large structural fluctuations that contribute to the remarkable properties of LHP-based optoelectronic devices. In three-dimensional LHPs such as $CH_3NH_3PbBr_3$, the structural phase transitions have been well characterized; changes in local structure and origins of structural disorder, however, have received less attention. We investigate the temperature dependence of the Pb—Br bond distribution, effective spring constant, and dynamic correlations with a combined extended x-ray-absorption fine structure (EXAFS), single-crystal x-ray diffraction (SXRD) and *ab initio* molecular dynamics (AIMD) study. EXAFS provides a snapshot of the local environment around the probe atom, rather than the time- and space-averaged structure obtained from SXRD. Molecular librations are observed below the orthorhombic-tetragonal transition temperature, and across this transition we find an anomalous increase in the Pb-Br effective spring constant. The x-ray absorption near edge structure reveals only subtle changes in the electronic structure; therefore, we propose that the increase in bond strength is the result of a redistribution of the charge density, concomitant with the loss of persistent Br…H bonding. Furthermore, the temperature dependence of the Pb—Br bond asymmetry indicates that the structural disorder in $CH_3NH_3PbBr_3$ is primarily driven by thermally activated anharmonic dynamics rather than static disorder. Our results describe the local structure responsible for the optoelectronic performance of LHP devices and bring new insights into modifying halide bonding to prevent halide migration.

DOI: 10.1103/PRXEnergy.2.033004

*Corresponding author. nicholas.weadock@colorado.edu

I. INTRODUCTION

Metal halide perovskite semiconductors (MHPs) have attracted much attention for application in optoelectronic devices. The primary research focus of MHPs has been as solar absorbers, with device efficiencies recently exceeding 25.5% [1,2]. This high efficiency is explained by the relevant optoelectronic properties of MHPs: they possess a tunable band gap, sharp optical absorption edge, low rate of nonradiative recombination, long carrier diffusion length, and reasonable charge carrier mobility [3–5]. What is remarkable is that these optoelectronic properties are achieved in materials with strongly anharmonic lattice dynamics, facile halide migration, and a structure with significant disorder [3,6].

Bulk MHPs have the stoichiometric perovskite formula ABX_3, with common A-site cations including methylammonium ($CH_3NH_3^+$, MA^+), formamidinium [$CH(NH_2)_2^+$, FA^+], or Cs^+, B-site cations including Pb^{2+} or Sn^{2+}, and halides (Cl^-, Br^-, I^-) as the X-site anions. X-ray and neutron diffraction experiments show well-resolved crystal structures; the majority of MHPs are orthorhombic at low temperatures, then transition to a tetragonal and cubic phase with increasing temperature [7–11]. These phase transitions are displacive and proceed by successive tilting of metal-halide octahedra along different crystallographic axes. For organic-inorganic hybrid MHPs, organic A-site cations can unlock from well-defined positions and begin librating and rotating at the orthorhombic-tetragonal transition and are disordered within the cubic phase. This behavior has been well characterized in MA^+-containing MHPs [7,8,12]. The global phase transitions in $MAPbBr_3$ are at $T \sim 147$ K (orthorhombic to tetragonal) and $T \sim 236$ K (tetragonal to cubic). The transition from orthorhombic includes an intermediate incommensurate tetragonal phase over a narrow temperature range [13–16]. Single-crystal neutron diffraction experiments, which have a higher sensitivity to C, N, and H, identified a second, low-temperature incommensurate phase within the MA^+ sublattice [15].

The majority of research on MHP solar absorbers has focused on hybrid lead halide perovskites (LHPs), with the highest efficiency perovskite solar cells utilizing alloys based on lead-iodide perovskite absorber layers [1,17]. Compared to the iodides, lead-bromide perovskite-based solar absorbers have lower peak efficiencies but larger band gaps and have proven to be more resistant to degradation [18]. This larger band gap leads to a higher open circuit voltage device [19,20] and shows promise in tandem device applications [21]. The inclusion of robust $MAPbBr_3$ into a $FAPbI_3$-based device improved both the stability and optoelectronic performance, suggesting a successful path to commercial devices [22].

Recent computational studies have connected key optoelectronic properties in hybrid LHPs, including the ideal optical absorption onset and long charge carrier lifetimes, to the large structural disorder in the device-relevant cubic phases [4,12,23]. This disorder can also modify the barriers to halide migration, a known cause of LHP device degradation [24]. Experimentally, disorder in LHPs manifests as large anisotropic thermal displacement parameters (ADPs) [3]. In neutron and x-ray scattering experiments, large ADPs reduce the intensity of Bragg peaks and increase the width of peaks in a pair-distribution function through the Debye-Waller factor. Beyond the large ADPs, however, there is a discrepancy between the long-range order (measured with diffraction) and local order in cubic LHPs. X-ray and neutron total scattering experiments on cubic LHPs find reduced local symmetry within a few unit cells [25–28], with a recent study identifying dynamic, two-dimensional structural correlations in $MAPbI_3$ and $MAPbBr_3$ [29]. A room-temperature extended x-ray-absorption fine structure (EXAFS) comparison of the Pb—Br bond dynamics in $CsPbBr_3$ and $FAPbBr_3$ found signatures of dynamic Pb-Br disorder in both compounds, dynamics that are further modulated by hydrogen bonding in the case of $FAPbBr_3$ [30].

The origin of structural disorder in LHPs has been widely investigated and may contain contributions from anharmonic interatomic potentials [26,31,32], point defects [33], Pb lone-pair-driven off-centering [27], or polymorphous ground states [23]. These contributions can be distinguished by their temperature dependence; disorder due to anharmonicity is expected to grow continuously with increasing temperature, whereas disorder from point defects or a complex ground state will be significant even at low temperatures. A recent EXAFS analysis of $MAPbI_3$, $MAPbCl_3$, and chloride-substituted $MAPbI_3$ found significant lead-halide bond anharmonicity for both halides, pointing to anharmonicity as a significant contributor to disorder in MA-based LHPs [34].

In this study we investigate the temperature-dependent local and long-range structure of $MAPbBr_3$ through a combined analysis of EXAFS, single-crystal x-ray diffraction (SXRD) experiments, and *ab initio* molecular dynamics (AIMD) simulations. The temperature-dependent EXAFS spectra are analyzed with a cumulant expansion to extract bond lengths and pairwise thermal displacement parameters and reveal asymmetries in nearest-neighbor pair-distribution functions (PDFs). In this article, PDF refers to the pair-distribution function obtained from EXAFS measurements unless otherwise defined. Comparison with SXRD results yields further insight into the correlated motions of the nearest neighbors [35–38]. We find that the structural disorder in $MAPbBr_3$ has a significant thermal component, arising from a dynamic exploration of an anharmonic potential landscape. The structural changes associated with the orthorhombic-to-tetragonal transition are accompanied by an anomalous increase in the Pb–Br effective spring constant. The origin of this increase is

investigated with x-ray-absorption near-edge spectroscopy (XANES) and proposed to be a subtle redistribution of the charge density. These changes in Pb—Br bonding contribute to the picture of the anharmonicity in $MAPbBr_3$ that governs the thermal and optoelectronic properties.

II. STRUCTURE DETERMINATION WITH X-RAY DIFFRACTION

The crystal structure of $MAPbBr_3$ is solved from SXRD measurements at several temperatures ranging from 100–300 K. Details of the refinement are provided in Appendix A 2, and the resulting crystallographic information files (CIFs) and comparisons to existing literature are provided as Supplementary Material [39] (with additional references therein [40–42]) and illustrated in Supplementary Material Fig. S1. The structure of $MAPbBr_3$ is refined in the orthorhombic *Pnma* phase from 100–145 K, the tetragonal $I4/mcm$ phase from 155–230 K, and the cubic $Pm\bar{3}m$ phase from 240–300 K. The structure solutions we obtain are used as the initial structures for EXAFS analysis of samples 1 and 2 (termed samples S1, S2) and AIMD simulations, both described in detail below. Figure 1(a) plots R_C, the Pb—Br bond lengths obtained from SXRD, compared with the EXAFS Pb—Br bond length r_{avg}. We observe subtle differences in R_C in the orthorhombic and tetragonal phases for each crystallographically distinct Br atom, indicating a slight distortion of the $PbBr_6$ octahedra. These differences are too small to be resolved in EXAFS. In SXRD, the R_C is calculated as the distance between average atom positions, whereas in EXAFS r_{avg} is an average of instantaneous bond lengths that include contributions from transverse displacements. The relationship between r_{avg} and R_C is provided in Eq. (A4), which shows that r_{avg} is greater than R_C. We also plot the SXRD- and EXAFS-equivalent bond lengths, R_C^{MD} and $r_{\mathrm{avg}}^{\mathrm{MD}}$, calculated from our AIMD simulations (using the FHI-aims code [43] and the Perdew-Burke-Ernzerhof [44] density functional together with the Tkatchenko-Scheffler [45] dispersion correction; see Appendix A 4 for details) according to Eqs. (A5) and (A6). The AIMD bond lengths show close agreement with experiment and reproduce the temperature dependence.

Anisotropic thermal displacement parameters (ADPs) for each atom are obtained from the SXRD refinements and AIMD simulations. In Fig. S2 within the Supplementary Material [39], we plot the components of the Br ADPs that are parallel and perpendicular ($U_\parallel$, $U_\perp$) to the Pb—Br bond directions. These values are calculated following the procedure outlined by Downs [46]. As detailed in Appendix A 3, the correlated motions of neighboring Pb-Br atoms can be inferred from a comparison of $U_\parallel$ and $U_\perp$ to the mean-square relative displacements, σ^2 and $\sigma_\perp^2$, obtained directly from EXAFS fits and from Eq. (A4). This comparison yields correlation coefficients $\phi_\parallel$ and $\phi_\perp$,

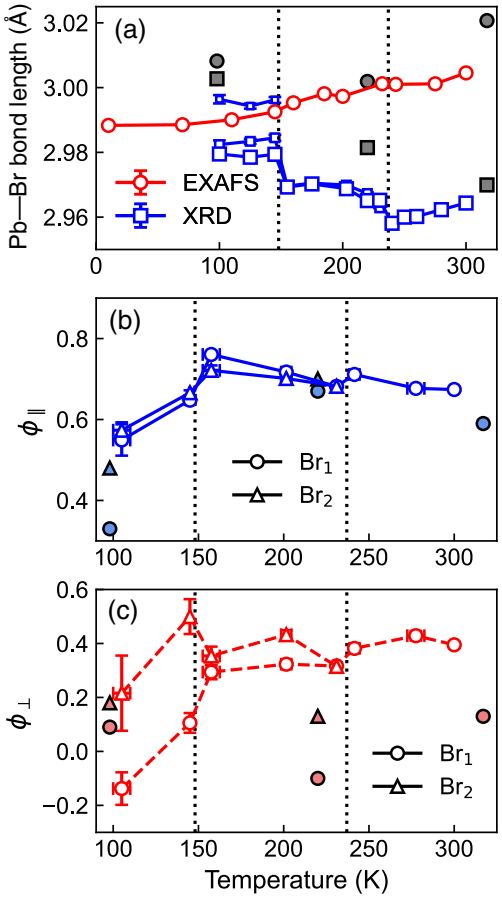

FIG. 1. (a) Pb—Br bond lengths obtained from EXAFS sample S2 (circles) and SXRD (squares), where SXRD reports different bond lengths for the three crystallographically distinct Br sites in the orthorhombic phase, and two sites in the tetragonal phase. Equivalent values calculated from AIMD simulations included in gray, with SXRD an average of each Br site. Note that small systematic errors between bond lengths from the density functional used and bond lengths from diffraction experiments are expected at the scale resolved here. Correlation coefficients for atomic displacements parallel (b) and perpendicular (c) to the Pb—Br bond for crystallographically distinct Br atoms. The correlation coefficients are only calculated for SXRD and EXAFS data points that are within 5 K of each other. Correlation coefficients $\phi_\parallel^{\mathrm{MD}}$ and $\phi_\perp^{\mathrm{MD}}$ calculated from AIMD are plotted as blue- and red-filled symbols, respectively. Experimental error bars may be smaller than the corresponding symbol. Error bars for EXAFS bond lengths in (a) are the relative error bars between temperature points.

defined by Eqs. (A2) and (A3), which describe the degree of correlated motion between neighboring atoms parallel and perpendicular to the bond direction. For purely correlated motion, the pair of atoms move entirely in phase ($\phi = 1$), while anticorrelated motion describes out-of-phase atom displacements ($\phi = -1$) [38]. A schematic of the parallel and perpendicular correlated motions of the Pb-Br atom pair is provided in Supplementary Material Fig. S3.

Figure 1(b) plots Pb-Br $\phi_\parallel$ and $\phi_\perp$ calculated from Eqs. (A2) and (A3). At all temperatures, parallel motion is moderately to highly correlated. Initially, $\phi_\parallel$ increases with the transition from the orthorhombic to tetragonal phase, which is unusual, before declining slightly with increasing temperature above 150 K. The correlation coefficient $\phi_\perp$ is low for all temperatures; it increases at the orthorhombic-tetragonal transition and then changes little from 150 to 300 K. We also calculate and plot Pb-Br correlation coefficients from our AIMD simulations, $\phi_\parallel^{\mathrm{MD}}$ and $\phi_\perp^{\mathrm{MD}}$, using Eqs. (A2)–(A4), (A7), and Eq. (S7) within the Supplementary Material [39]. The AIMD $\phi_\parallel^{\mathrm{MD}}$ is in good agreement with experimental values. The agreement between $\phi_\perp$ and $\phi_\perp^{\mathrm{MD}}$ is less good, likely a result of the small supercell AIMD simulations that may not correctly capture longer wavelength phonons. A discussion of this discrepancy is provided in Sec. III within the Supplementary Material [39].

III. EXAFS DATA AND ANALYSIS

A. *k*-space and *r*-space data

The *k*-space EXAFS data at the Pb L_{III} edge are plotted in Fig. 2(a). They exhibit a novel behavior that is not often seen so clearly in raw *k*-space data, and often not observed at all up to 300 K. Specifically, the data show an accordionlike effect in which the zero crossings in *k*-space shift to higher *k* with increasing temperature and the magnitude of the shift increases with *k*. The shift of the zero crossings is highlighted in Fig. S4 within the Supplementary Material [39], which presents an expanded view of the Pb L_{III}-edge *k*-space data. This behavior is a clear sign of increasing asymmetry in a PDF. The *k*-space EXAFS data are modeled with a cumulant expansion [35,47,48]. When terms up to k^4 are included in this expansion, the EXAFS function for the Pb-Br pair, $k\chi_{\mathrm{Pb\text{-}Br}}(k)$, has the form

$$k\chi_s(k,r) = A_1 \sin\left(2kr - \frac{4}{3}C_3k^3 + \phi(k)\right), \tag{1a}$$

$$A_1 = \frac{NS_0^2}{r^2}F(\pi,k)e^{-2r/\lambda(k)+2C_4k^4/3}, \tag{1b}$$

$$k\chi_{\mathrm{Pb\text{-}Br}}(k) = \int_0^\infty g(r,r_{\mathrm{avg}})k\chi_s(k,r)dr. \tag{1c}$$

Here N is the number of Br neighbors, S_0^2 is the amplitude reduction factor, F is the backscattering amplitude of the photoelectron wave, λ is the mean free path (the term $e^{-2r/\lambda(k)}$ is often combined together with F), $\phi(k)$ is a known phase factor arising from the excited and backscattering atoms (calculated using FEFF7 [49]), $g(r,r_{\mathrm{avg}})$ is the PDF centered at r_{avg} (the variance of this function, σ^2, is usually called the Debye-Waller factor), and C_3 is proportional to the skewness of the PDF, a measure of the asymmetry [35,47,48]. The C_3k^3 term produces the stretch of the waveform in *k*-space; see Fig. 2(a). The term involving C_4 is a small correction to the amplitude that is proportional to the kurtosis.

Figure 2(b) plots fast Fourier transforms (FFTs) of the Pb L_{III}-edge *k*-space data to *r*-space with peaks corresponding to various shells of neighbors about the excited atom. In such *r*-space plots, the fast oscillation is the real part *R* of the FFT, while the envelope function is $\pm\sqrt{R^2+I^2}$, where *I* is the imaginary part of the FFT. The dominant peak is the nearest-neighbor Pb-Br peak near 2.6 Å; several weak overlapping Pb-N and Pb-C peaks

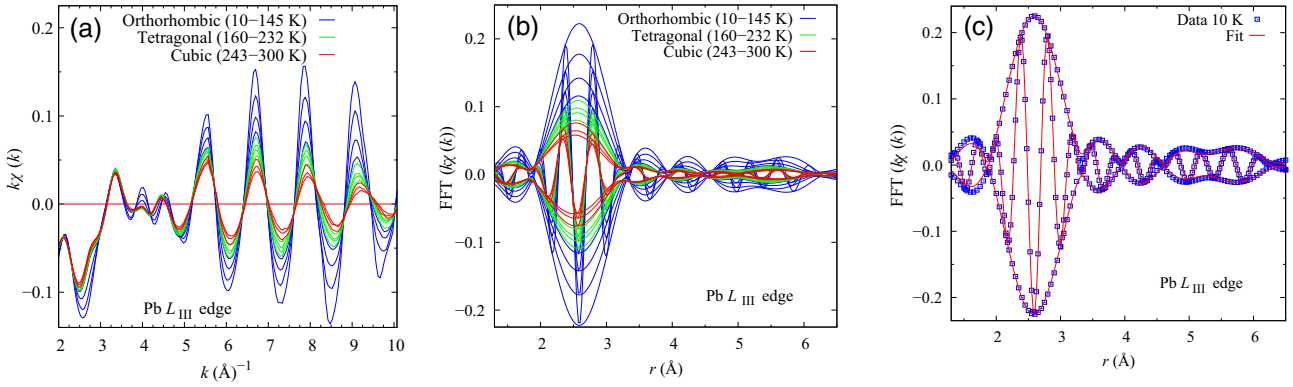

FIG. 2. (a) Pb L_{III}-edge data from sample S1 in *k*-space that exhibits an unusual temperature dependence. Upon close inspection of the zero crossings, the accordion effect associated with an asymmetric distribution is evident; at high *k*, the positions of the zero crossings move to higher *k* as temperature increases and the wave pattern is stretched. (b) Temperature-dependent Pb L_{III} *r*-space data obtained from FFT of *k*-space data; blue lines (10, 70, 110, 145 K) are the traces for the orthorhombic phase, light green lines (160, 185, 200, 232 K) are the traces for the tetragonal phase, and red-orange lines (243, 275, 300 K) are the traces for the cubic phase. The fast oscillation is the real part *R* of the FFT, while the envelope function is $\pm\sqrt{R^2+I^2}$, where *I* is the imaginary part of the FFT. The FFT range is 3.5–10.0 Å^{-1}, Gaussian rounded by 0.2 Å^{-1}. The multiscattering peaks dominate the 5.3–5.9 Å range. (c) Example of a fit to the 10-K Pb L_{III}-edge data over the *r* range 1.6–6.3 Å and using the same FFT range as in (b).

combine to form the structure from 4–5.3 Å, and the small peak near 5.6 Å is a combination of a Pb-Pb peak, a weak, second Pb-Br peak, plus several multiscattering peaks such as Pb-Br-Pb-Br-Pb. The Pb-C and Pb-N pairs are identified by average bond lengths because EXAFS cannot discriminate between weak N and C backscatterers. Note that the Pb-C and Pb-N peaks damp rapidly with increasing temperature and can only be investigated in the orthorhombic phase. For $T > 150$ K, the tail of the nearest-neighbor Pb-Br peak is the primary contribution to the EXAFS amplitude from 3.3–4.8 Å.

We also perform Br K-edge EXAFS measurements, which require removal of underlying Pb L_{III} oscillations, as shown in Supplementary Material Fig. S5 [39]. The k-space and r-space data are plotted in Supplementary Material Fig. S6. The amplitude of the k-space data is reduced by the reduction in the number of nearest neighbors and partial destructive interference caused by the crystallographically distinct Br sites. Despite the reduced signal to noise of the Br K-edge data, we still observe the shift in zero crossings of the k-space data in Supplementary Material Fig. S6(a) and perform an FFT to the r-space data in Supplementary Material Fig. S6(b).

B. Fits

We extract the three parameters defining the atomic PDFs (r_{avg}, σ^2, and C_3) by fitting a sum of EXAFS functions to the Pb and Br r-space data. The number of neighbors is fixed to the values from the structure. We measure S_o^2 at low temperature for several samples and fix it at a value of 0.994 for the Pb L_{III} edge. The C_4 parameter is negligible except at the highest temperatures. A representative fit to the 10-K Pb L_{III}-edge data is provided in Fig. 2(c). EXAFS functions are calculated using FEFF7 [49] for each atom pair in a given structure corresponding to the space groups obtained from SXRD. EXAFS cannot resolve peaks that are split by less than 0.15 Å for an FFT range up to 10 $Å^{-1}$ for the Pb L_{III} edge; therefore, slightly split peaks are treated as a single peak. For example, although the nearest-neighbor Pb-Br peaks are slightly split in the orthorhombic phase, a single EXAFS function is used with an amplitude of six neighbors. Additional details of fits to the Pb L_{III} edge and Br K edge are presented in the Supplementary Material [39]. Because the first Pb-Br peak is quite well separated, 1-peak fits are also performed over the restricted range 2–3.1 Å; three parameters are varied, r_{avg}, σ^2, and C_3, and three degrees of freedom remain [50]. Figure 1(a) plots r_{avg} along with R_C; the σ^2 and C_3 results are discussed below.

1. σ^2 and bonding

The results for $\sigma^2(T)$ obtained for the nearest-neighbor Pb-Br and Br-Pb pairs are shown in Figs. 3(a) and 3(b). The results are nearly identical for the two edges and are very reproducible, with error bars calculated from three separate measurements. Surprisingly, the values do not follow a correlated Debye (or Einstein) model over the entire temperature range; specifically, the plots show a change in slope near 145 K. The correlated Debye model used to model the data is expressed as

$$\sigma^2_{cD} = \frac{3\hbar}{2M_R}\int_0^{\omega_D}\frac{\omega}{\omega_D^3}C_{pair}\coth\left(\frac{\hbar\omega}{2k_BT}\right)d\omega + \sigma^2_{static}, \quad (2)$$

where M_R is the reduced mass, ω_D is the Debye frequency, and C_{pair} is a correlation function defined as $1 - \sin(\omega r_{avg}/c)/(\omega r_{avg}/c)$ with $c = \omega_D/k_D$ and k_D the Debye wave vector.

Fits to a correlated Debye model are then performed (for both samples and edges) over two temperature ranges, 0–145 K and 145–300 K; these are shown as solid lines in Figs. 3(a) and 3(b) with dotted lines showing an extension of the low- or high-temperature fits. The static component of σ^2 increases from $\sigma^2_{static} = 0.000\,35(5)$ $Å^2$ in the low-temperature range to $\sigma^2_{static} = 0.0023(7)$ $Å^2$ in the high-temperature range. From this we extract a very small static disorder, $\sqrt{\sigma^2_{static}}$, of 0.018(1) Å and 0.047(4) Å in the low- and high-temperature ranges, respectively. The correlated Debye temperatures, Θ_{cD}, from these fits are 148 ± 4 K for low temperature and 167 ± 5 K above 150 K. We use the temperature dependence of σ^2 to estimate the effective spring constant of the bond. In the high-temperature limit

$$\kappa = k_B/(\partial[\sigma^2]/\partial T), \quad (3)$$

where κ is the effective spring constant for the pair that includes interactions with other neighboring atoms. It can be obtained from the inverse slope of the σ^2 versus temperature plot at high temperature. The values of $\kappa_{Pb\text{-}Br}$ from these fits are 1.43 eV/$Å^2$ and 1.87 eV/$Å^2$ for low and high temperatures, respectively. These values are consistent with other reported lead-halide κ values of 1.47 eV/$Å^2$ for $CsPbI_3$, 1.32 eV/$Å^2$ for $MAPbI_3$, and 1.75 eV/$Å^2$ for $MAPbCl_3$ [28,34]. We note that none of these studies resolved a change in κ across the orthorhombic-tetragonal transition. Figure S7(a) within the Supplementary Material [39] compares the temperature dependence of σ^2 for $MAPbBr_3$ to that reported for $MAPbCl_3$ and $MAPbI_3$ [34]. Above 75 K, σ^2 increases slightly with halide mass. We also estimate the transverse effective spring constant $\kappa_\perp$ by fitting Eq. (2) to the temperature dependence of $\sigma^2_\perp$ [see Eq. (A4)]. The results are shown in Supplementary Material Fig. S8. Low-temperature values for $\sigma^2_\perp$ are calculated using R_C reported by Swainson *et al.* [8]. The obtained $\kappa_\perp = 0.11$ eV/$Å^2$ is extremely small (a factor of 10 less than κ) and consistent with $\kappa_\perp = 0.31$ eV/$Å^2$ reported for $MAPbI_3$ [34].

Figure 3(c) plots σ^2 for the Pb-N and Pb-C pairs. The data point for the Pb-N pair (green) at 145 K is 0.063 $Å^2$,

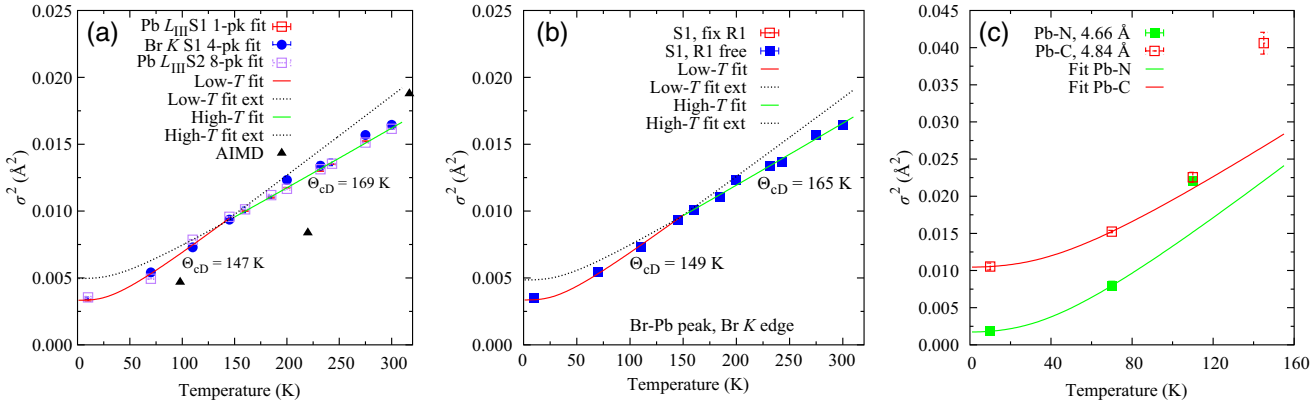

FIG. 3. The σ^2 for the first neighbor pair at each edge as a function of temperature: (a) Pb-Br from the Pb L_{III} edge with one plot for Br-Pb (blue circles) for comparison of the two edges, (b) Br K edge for two different analyses. R1 is the Pb–Br bond length parameter varied in the fits, yielding r_{avg} at each temperature. In the second set of fits for σ^2, R1 is fixed to values obtained from a linear fit of $r_{avg}(T)$. The broadening with temperature is nearly identical for the two edges and is not sensitive to small variations in the bond length r_{avg}. The curves show a change in slope near 145 K, and do not fit a correlated Debye (or Einstein) model over the entire temperature range. Fits over restricted temperature ranges, 0–145 K and 145–300 K, agree well with the data and are identical within errors for the two edges; the Debye temperature for the orthorhombic phase is 148 ± 4 K while that for higher temperatures is 167 ± 5 K. No obvious change in slope is present at the tetragonal-to-cubic phase transition near 240 K. In (c) the low-temperature σ^2 results for the first two Pb-C and Pb-N peaks from sample S1 are shown—these small peaks occur near 4.1 and 4.3 Å in Fig. 2(b) (actual distances 4.66 and 4.88 Å), and damp rapidly with temperature. Simple correlated Debye or Einstein models do not fit as σ^2 increases much too rapidly above 100 K; note that σ^2 at 145 K for the 4.66-Å peak (green) is far off scale. The value at 145 K for Pb-N is 0.063 Å^2, which is too large to be meaningful. Restricted correlated Debye model fits (solid lines) of the lowest two data points for each bond length suggest a moderate Θ_D of order 240 K. In (a), the σ^2_{MD} values obtained from AIMD simulations [Eq. (S6) within the Supplementary Material [39]] are plotted as solid triangles, showing reasonable agreement with the experiments.

which is too large to be meaningful. Correlated Debye (or Einstein) models can be fit to the lower two data points with a correlated Debye temperature of order 240 K for Pb-C; the effective spring constant is correspondingly weak, of order 0.5 eV/Å^2. The effective spring constant is a combination of any direct attraction or repulsion plus contributions from surrounding atoms. As a result, it is possible to obtain a positive κ despite the cationic nature of both Pb^{2+} and MA^+. The rapid rise in σ^2 above about 100 K, however, is not consistent with either a Debye or Einstein model. The dramatic increase in σ^2 is concomitant with a reduction in amplitude in the r-space data between 4 and 4.6 Å [Fig. 2(b)] in the orthorhombic phase EXAFS; it is likely indicative of a break in hydrogen bonds between the MA^+ ion and the $PbBr_6$ sublattice. At higher temperatures in the tetragonal or cubic phases, changes in the amplitude of this peak cannot be measured.

2. C_3 and asymmetry

Figure 4 plots the C_3 parameter for the Pb-Br peak as a function of temperature. The obtained parameters follow the expected T^2 dependence [51–53], and the value at 300 K is an order of magnitude larger than observed for other semiconductors [53]. Setting $C_3 = 0$ in fits of the EXAFS data results in a poor fit, indicating that asymmetry in the PDF is significant. At low temperature, the small C_3 values arise from zero-point motion within an anharmonic potential [51–53]. The asymmetry to the high-r side becomes significant at 300 K. We isolate the asymmetry in the Pb—Br bond with a back FT of the r-space Pb-Br and Br-Pb peaks in Fig. S9 within the Supplementary Material [39]. This back FT also exhibits shifts in the zero crossing of k-space data, visible even within the orthorhombic phase. We quantify the shift in zero crossings of the back FT in Supplementary Material Fig. S10 and see an increase with temperature as expected from the C_3 behavior. Supplementary Material Fig. S7(b) compares the Pb-Br C_3 parameter with those previously reported for Pb-I and Pb–Cl. Below 150 K, C_3 increases slightly with halide mass at a given temperature; however, the scatter in reported C_3 for Pb-I and Pb–Cl at high temperatures makes the trend less clear [34].

C. XANES

We characterize the Pb L_{III} and Br K-edge XANES to investigate any possible electronic structure changes of the Pb and Br ions, motivated by the change in effective spring constant of the Pb—Br bond. The Pb and Br full XANES spectra, plotted in Fig. S11 within the Supplementary Material [39], show no shifts of the edges (within 0.15 eV), only changes in amplitude with temperature. The top of the Pb L_{III} edge, plotted in Supplementary Material Fig. S12(a), has an oscillation at 13 057 eV that

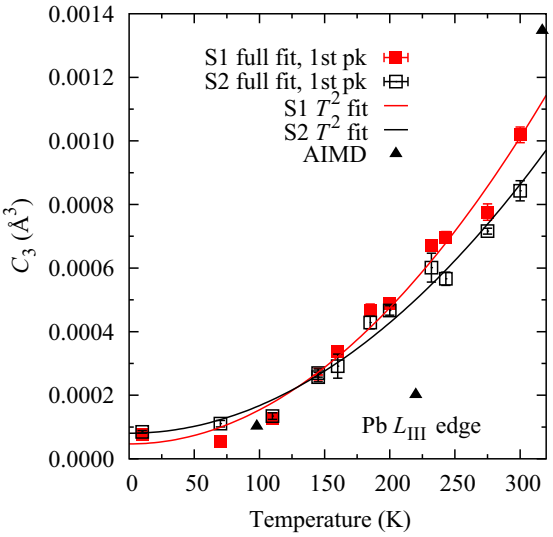

FIG. 4. The C_3 parameter for the Pb-Br peak as a function of temperature for both samples. Generally, C_3 varies as T^2; [35] the two lines show a T^2 fit for each sample, and fit the data well within the fluctuations. The C_3 values obtained from AIMD simulations [Eq. (S6) within the Supplementary Material [39]] are denoted with solid triangles.

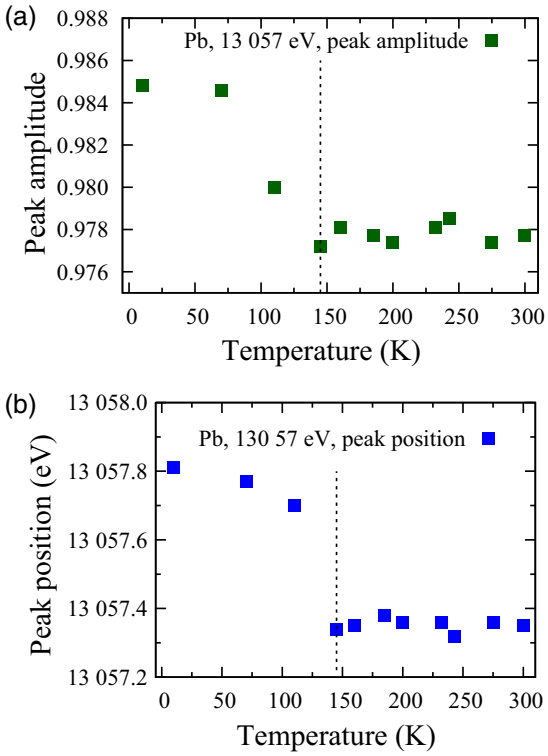

FIG. 5. Temperature dependence of the peak amplitude (a) and position (energy) (b) for the peak near 13 057 eV in the Pb XANES plots from sample S2 (see Fig. S12 within the Supplementary Material [39]). The amplitude of this peak stays nearly constant up to 70 K and then falls rapidly with increasing temperature to 145 K; above 145 K, it remains essentially constant. The peak position also shifts to lower energy with increasing temperature, mostly between 70 and 145 K, but then remains constant at all higher temperatures. The vertical dashed line indicates the orthorhombic-tetragonal transition temperature.

exhibits significant changes across the orthorhombic-to-tetragonal transition. Figure 5 plots the temperature dependence of the amplitude and position of this oscillation near 13 057 eV (from 13 053 to 13 065 eV). Both the amplitude and position decrease strongly with temperature in the orthorhombic phase before achieving steady state in the tetragonal and cubic phases.

The Br K-edge XANES in Fig. S12(b) within the Supplementary Material [39] exhibits a large peak centered near 13 477 eV. The amplitude of this peak, plotted in Supplementary Material Fig. S13, decreases linearly with temperature through all three phases with no indications of the phase transitions. The magnitude of the change is greater than observed for Pb and reflects the large transverse motion of Br. This large decrease, however, could mask a small discontinuity at the phase transition. Additional changes in the Br XANES, outlined in the Supplementary Material, are all gradual. Thus, the detectable electronic structure changes that correlate with the orthorhombic-tetragonal transition are associated with the Pb^{2+} ions.

IV. AIMD RESULTS

AIMD simulations provide a unique view of the dynamics that are spatially averaged out in EXAFS and XRD measurements. Supplementary Videos 1–3 [39] visualize the dynamics of $MAPbBr_3$ at three temperatures, 98, 220, and 317 K, corresponding to the orthorhombic, tetragonal, and cubic phases. These simulations are used to calculate the SXRD- and EXAFS-equivalent Pb—Br bond lengths, $r_{\text{avg}}^{\text{MD}}$ and R_C^{MD}, and correlation coefficients $\phi_\parallel$ and $\phi_\perp$ for direct comparison to the experimental results in Fig. 1. The AIMD simulations correctly capture the temperature dependence of all four parameters, indicating that the simulations provide a qualitatively accurate representation of the $MAPbBr_3$ structure. Note that some systematic prediction errors of absolute bond lengths [Fig. 1(a)] are expected as a consequence of the use of an approximate density functional (even for the static structure); what is important is that the trends of dynamical averages with temperature agree. We further parameterize aspects of the dynamics specific to neighboring $PbBr_6$ octahedra and the hydrogen bond between MA^+ molecules and Br^- in Fig. 6 and Figs. S16–S19 within the Supplementary Material [39], respectively. Joint probability contour plots in Figs. 6(b)–6(d) relate the Pb—Br—Pb bond angle and Pb—Pb pair distance for neighboring octahedra. In the orthorhombic phase at 98 K, the distribution exhibits a peak at 153° and 5.87 Å with a tail extending to a higher

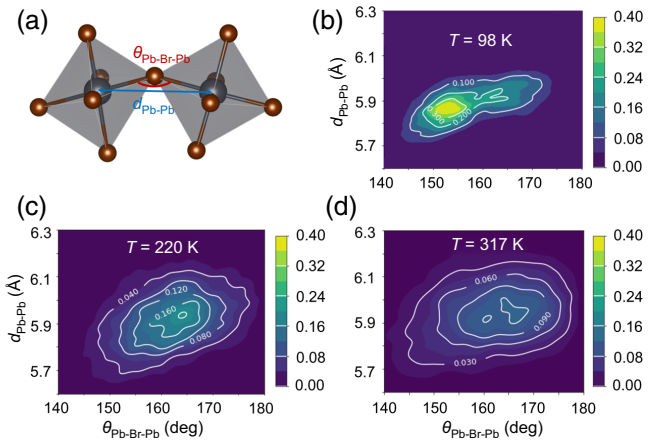

FIG. 6. (a) Schematic denoting the Pb—Br—Pb bond angle and Pb—Pb distance used to parameterize $PbBr_6$ disorder in AIMD simulations. Correlated bond angle and bond distance contour plots in the (b) orthorhombic phase at 98 K, (c) tetragonal phase at 220 K, and (d) cubic phase at 317 K. Colorbars indicate the probability of occurrence. The bond angle is defined such that the value never exceeds 180°.

angle and bond distance. The peak is consistent with neighboring $PbBr_6$ octahedra that are largely locked into tilted configurations across shared corners, bringing the central Pb atoms closer together. The tail towards higher Pb—Br—Pb angles corresponds to octahedral rotations that straighten the bond and therefore increase the Pb—Pb distance, but this straightening happens relatively infrequently. In the tetragonal and cubic phases [Figs. 6(c) and 6(d)], however, the peak smears out and the centroid shifts to a higher bond angle and bond length, indicating that the octahedra lose their preference for strongly tilted configurations in either phase, preferring to occupy a broader phase space with fewer dynamic constraints on the tilt angle instead. Overall, the clear change related to the $PbBr_6$ network that occurs between the orthorhombic and tetragonal phases, but not nearly as pronounced between the tetragonal and cubic phases, is consistent with the Pb—Br bonding–related changes seen in XANES L_{III}-edge data in Fig. 5.

The MA^+ dynamics are visualized in Figs. S16–S19 within the Supplementary Material [39]. Supplementary Material Fig. S16 plots density maps of the C, N atom positions for all three phases. These positions are localized in the orthorhombic phase; however, in the tetragonal and cubic phases they reflect the dynamic molecular motions reported previously [12,54,55]. We also track Br…H bond dynamics in Supplementary Material Figs. S17–S19(c)–(f), which plot the time dependence of the Br…H bond length. We consider a hydrogen bond to be approximately defined for Br…H distances less than 3 Å, the van der Waals limit for Br…H [56]. In the orthorhombic phase, this corresponds to each Br forming one hydrogen bond with a $-NH_3$ group and one bond with a $-CH_3$ group from a different MA^+ cation; these hydrogen bonds remain in place over the full length of the AIMD trajectory.

In the tetragonal and cubic phases the persistent Br…H—N bonds disappear. Instead, we observe the formation of transient Br…H—N bonds, marked by instances when the Br…H—N distance for one hydrogen in a single $-NH_3$ group drops below 3 Å. In the AIMD trajectory associated with the tetragonal phase (conducted at $T \approx 220$ K), these occasionally formed hydrogen bonds persist for time durations of about 1–2 ps. For the even higher-temperature cubic phase (AIMD simulation conducted at $T \approx 317$ K), the fluctuation of all Br…H bond lengths is much larger than in the tetragonal or orthorhombic cases. However, the lack of persistent hydrogen bond formation is similar between both the tetragonal and cubic phases, with only very occasional hydrogen bond formation over perhaps 1–2 ps observed in our corresponding $T \approx 317$ K AIMD trajectory. The Br…H—C bond is weaker than the Br…H—N bond, and does not seem to form any discernible hydrogen bonds in the tetragonal or cubic phases at all [57].

We also construct the nearest-neighbor Pb-Br PDF at all three simulation temperatures in Fig. S20 within the Supplementary Material [39]. The 317-K distribution shows significant asymmetry towards longer bond lengths. Analogues to EXAFS cumulants, σ^2_{MD} and C_3^{MD} are calculated from these AIMD distribution functions and are plotted in Figs. 3 and 4, respectively. Although quantitatively smaller, they show qualitatively similar trends with the experimentally determined values. One possibility for why the AIMD values are found to be overall lower is the fixed supercell boundaries used in the simulations, which could restrict longer-range anharmonic motion in the Pb-Br sublattice associated with nonlocal expansions and contractions of lattice regions as a whole.

V. DISCUSSION

Below, we outline how the temperature dependence of the structural disorder indicates that this disorder is primarily dynamic with little static contributions. In addition to structural changes, we observe bonding changes that result in an anomalous stiffening of the Pb—Br bond. Finally, we outline the role of anharmonicity in determining the local structure, even at low temperatures.

A. Thermal evolution of disorder

We parameterize structural disorder through the temperature dependencies of σ^2, C_3, and Br ADPs in Figs. 3, 4, and Fig. S2 within the Supplementary Material [39] and gain insight into the dynamics driving this disorder through $\phi_\parallel$, $\phi_\perp$, and AIMD simulations. In the low-temperature orthorhombic phase σ^2_{static} is extremely small, indicating

that disorder at finite temperatures is thermally driven. This result is consistent with recent analyses of photocurrent spectroscopy that found negligible static disorder in several LHP compounds [58]. The SXRD results reveal that orthorhombic $MAPbBr_3$ has well-defined octahedral tilts and MA^+ cation orientation. The 98-K structure simulated with AIMD is visualized in Supplementary Video 1 and reflects limited disorder. From this simulation we find that the correlated distribution of Pb—Br—Pb bond angles and Pb—Pb pair distances in Fig. 6(b) are sharply peaked near 153° and 5.87 Å, indicating limited octahedral rotational disorder within the $PbBr_6$ sublattice. Finally, the Br...H pair distances plotted in Supplementary Material Fig. S17 show little variation, maintaining the same Br...H bonds through the duration of the simulation.

Within the orthorhombic phase, the majority of the disorder comes from the MA^+ cation. The activation of librational modes of the MA^+ cation above 100 K, in which the C-N axis fluctuates in time, is inferred from the anomalous deviation of $\sigma^2_{\text{Pb-C/N}}$ with respect to the correlated Debye model fit in Fig. 3(c). C-N libration has also been inferred from hydrogen ADPs reported for $MAPbI_3$, and spectroscopically observed in inelastic neutron scattering and photoluminescence experiments [11,14,59,60]. For $MAPbBr_3$, low-energy "nodding donkey" modes, which involve partial MA^+ rotations about the C or N atom, coupled to the inorganic cage by hydrogen bonding with the halide, are analogous to the librational modes and show a well-defined spectral peak in neutron spectroscopy at low temperatures [7]. The mode lifetime begins to decrease at 75 K until the mode is no longer observed at the tetragonal phase transition [55]. We propose that $\sigma^2_{\text{Pb-C/N}}$ contains the amplitudes of the "nodding donkey" modes, and that the reduced lifetime observed in neutron scattering is related to the fluctuating strength of the Br...H bond modulated by thermal motion.

Above the orthorhombic-to-tetragonal transition (> 155 K), we observe several changes in the local structure. Notably, we see the loss of persistent hydrogen bonding in Fig. S18 within the Supplementary Material [39] as the Br...H—N bond distances begin to fluctuate greatly over time. The MA^+ cations exhibit libration and rocking of the C-N axis and hydrogen rotations about the C, N atoms, as seen in Supplementary Material Figs. S16(e) and S18(b), respectively. An increase in thermal disorder is apparent, particularly in the sharp increase of the Br $U_\perp$ seen in Supplementary Material Fig. S2, and a smearing out of the Pb—Br—Pb bond angles and Pb—Pb pair distance distribution in Fig. 6(c). The static rotation of neighboring octahedra with respect to one another (as inferred in the orthorhombic phase) is apparently no longer active in the tetragonal phase and, correspondingly, hydrogen bonds formed between MA^+ and Br^- can no longer be persistent. This general breaking up of locally persistent bonds also renders the individual MA^+ cations mobile in their respective cavities, imparting on them a freedom to rotate. We also observe an anomalous change in Pb—Br bonding, reflected in both the change in slope of $\sigma^2_{\text{Pb—Br}}$ and increase in $\phi_\parallel$ across the orthorhombic-tetragonal transition. Typically, nearest-neighbor correlations decrease with increasing temperature [37]. This behavior suggests an increase in the Pb—Br bond strength, discussed below.

Disorder increases through the tetragonal-cubic structural transition, identified here with XRD as occurring between 230 and 240 K. The octahedral tilts seen in Supplementary Videos 1 and 2 are no longer observed in Supplementary Video 3 [39]. There is a continuous increase in $\sigma^2_{\text{Pb—Br}}$ and C_3 with no change in slope (Figs. 3 and 4); however, there is a small discontinuity in $U_\perp$ (Fig. S2 within the Supplementary Material [39]). The correlated distribution in Fig. 6(d) is further smeared. The amplitude of MA^+ cation dynamics increase and there is a reduction in the lifetime of any transient Br...H—N bonds. These results suggest that, despite the global structural transition to the simple cubic phase, the local structural changes considered here reflect a continuous increase in the thermal disorder.

The Pb—Br bond disorder we characterize here is common among LHPs [27,30,32,34] and, at least in the case of MA^+-based LHPs, the disorder increases slightly with halide mass. Recent computational work has found that large amplitude iodine displacements impact several of the remarkable optoelectronic properties in $MAPbI_3$ [4]. Given that the Pb-I disorder is similar to Pb-Br and, to a lesser extent, Pb-Cl, we expect that the disorder in these LHPs should similarly affect their optoelectronic and other functional properties.

B. Bonding changes at the orthorhombic-tetragonal transition

The orthorhombic-tetragonal structural transition is accompanied by a remarkable 26% increase in $\kappa_{\text{Pb—Br}}$, suggesting that the Pb—Br bond has become stronger. Experimentally, we observe an increase in $\phi_\parallel$ and decrease in R_C. An increase in Pb-Br correlated motion, concomitant with a decrease in Pb—Br bond length, is consistent with a stronger Pb—Br bond. To understand the origin of this increase, we examine the Pb L_{III}-edge and Br K-edge XANES. Figure 5 shows a clear discontinuity in spectral weight and position of the top of the Pb L_{III} XANES across the structural transition. This trend indicates a redistribution in the charge density that shifts the Pb energy levels near the Fermi level. The exact nature of the shift cannot be determined from XANES. We hypothesize that the charge density redistribution results from the loss of persistent Br...H bonds and increases $\kappa_{\text{Pb—Br}}$. Such a redistribution would affect molecular orbitals with both bonding and antibonding character; the latter being particularly relevant to frontier orbitals at the valence band maximum (VBM)

and conduction band minimum (CBM). The change in the Pb—Br—Pb bond angle at the phase transition may also contribute to this shift, as previous work in related systems demonstrated that the positions of the VBM and CBM vary with metal-halide-metal bond angle [61–63]. Overall, the change in bonding is a more subtle effect than a change in ionicity of Pb^{2+} or Br^{-}, which would manifest as a shift of the main edge in the XANES spectra. The shifts of the main edge are of the order of 0.1 eV, too small for a change in oxidation state.

We examine the AIMD simulations to determine potential origins of the large Br $U_{\perp}$ in the tetragonal and cubic phases. The appearance of transient Br...H—N hydrogen bonds in the tetragonal and cubic phases does not strongly correlate with large transverse Br^{-} displacements. A careful examination of the steady-state dynamics in Supplementary Videos 1 and 2 [39] shows no obvious single origin of the jump in Br $U_{\perp}$; instead, we propose that the increase comes from a combination of factors, including an increase in thermal disorder within the $PbBr_6$ octahedra and the loss of persistent Br...H—N bonds, allowing for greater amplitude octahedral tilts. The increase in inter- and intraoctahedral disorder is evident in the broadened bond length-angle distribution of Fig. 6(c). The large variation in the Pb—Pb distance will also drive a large transverse Br motion irrespective of the strength of the Pb—Br bond, particularly for strong Pb-Pb correlations.

C. Pb—Br bond asymmetry

Asymmetry in the Pb-Br pair distribution function is observed qualitatively by the shift in zero crossings of the k-space data in Fig. 2 with increasing temperature, and quantified by C_3 in Fig. 4. The magnitude of the asymmetry is much greater than in traditional semiconductors; the C_3 for the Pb—Br bond in $MAPbBr_3$ at 300 K is an order of magnitude larger than that of the Ge—Ge bond at 600 K in pure Ge [64]. An asymmetric pair distribution function can arise from an anharmonic potential [28,65], but may also manifest from a split-site or off-centered model [27] that is static on the timescale of EXAFS (10^{-15} s) and has a splitting that is smaller than the experimental spatial resolution. To discern between the models, we consider the temperature dependence of the asymmetry parameter C_3. For a single-site anharmonic potential, C_3 has been shown to have a T^2 dependence [35]. This behavior is observed for $MAPbBr_3$ in Fig. 4. The off-centering distance in the cubic phase of LHPs varies linearly with temperature [27]. However, there is no model describing an explicitly linear temperature dependence of the off-centering. Therefore, given the T^2 dependence of C_3, we propose that an anharmonic potential in the Pb—Br bond is the dominant contributor to the asymmetric distribution function. Anharmonic potentials for Pb-halide bonds have been proposed for several other LHPs, although the consequences of this anharmonicity on structure and optoelectronic properties differ and require further investigation [28,34]. An in-depth analysis of the Pb-Br asymmetry, involving determination of C_3 using a new method involving the zero crossings, will be reported in a separate publication detailing the ambiguity of asymmetry in various nearest-neighbor pair distribution functions.

VI. CONCLUSIONS

The structural disorder in $MAPbBr_3$ is investigated with long-range (XRD) and local (EXAFS) structural probes and visualized with AIMD simulations. Our approach goes beyond the standard procedure of evaluating only the ADPs and instead determines the degree of local correlation and asymmetry. By utilizing a local approach, we directly probe the structural disorder that is known through computation to modulate the band gap and influence charge carrier lifetimes through the sampling of a dynamic energy environment. In particular, we find that the disorder possesses a significant thermal component. Additionally, the asymmetry in the Pb-Br pair distribution function suggests that thermal disorder originates from anharmonic interatomic potentials, manifesting even in the orthorhombic phase. At the local level, we corroborate the onset temperatures for librational motion in the MA^{+} cation and transverse Br^{-} motion enhanced by octahedral rotations. An enhanced understanding of the structural fluctuations will allow researchers to better understand and ultimately improve the remarkable optoelectronic properties of LHP devices.

We also uncover an anomalous change in the bonding character at the orthorhombic-tetragonal structural transition and onset of librational and rotational motion of MA^{+}. Through the transition, the effective spring constant of the Pb—Br bond increases 26%, from 1.44 to 1.82 eV/Å^2. This increase is reflected in the increase in correlation coefficient and decrease in XRD bond length across the structural transition. The change in spring constant likely arises from the breaking of Br...H bonds that shift the charge density in a way that increases Pb—Br bonding and alters the Pb energy levels. We note that the interatomic potentials are quite weak, even less than those for weakly bound "rattler" atoms in thermoelectric skutterudites [66]. A change in the Pb-Br effective spring constant will affect the diffusivity of Br^{-} and these results point to manipulating hydrogen bonding of the organic cation as a way to mitigate the detrimental effects of halide migration in LHP devices.

ACKNOWLEDGMENTS

The authors acknowledge fruitful discussions with David Cahen, who helped initiate this study. N.J.W. thanks anonymous reviewer C for their thorough analysis and guidance with regards to SXRD results. F.B. thanks Jason

Gruzdas for help in reducing data in the early stages of this project (EXAFS collection and analysis). N.J.W., L.W., J.A.V., M.F.T., X.Q., and V.B. (SXRD, data analysis, AIMD simulations) are supported by the Center for Hybrid Organic Inorganic Semiconductors for Energy (CHOISE), an Energy Frontier Research Center funded by the Office of Basic Energy Sciences, an office of science within the US Department of Energy (DOE). This research used resources of the National Energy Research Scientific Computing Center (NERSC), a U.S. Department of Energy (DOE) Office of Science User Facility operated under Contract No. DEAC02-05CH11231 (AIMD simulations). A portion of the research was performed using computational resources sponsored by the Department of Energy's Office of Energy Efficiency and Renewable Energy located at the National Renewable Energy Laboratory (AIMD simulations). J.A.V. acknowledges support from a Stanford University Office of the Vice Provost of Graduate Education fellowship and the National Science Foundation Graduate Research Fellowship Program under Grant No. DGE-1656518 (single-crystal synthesis). H.I.K. acknowledges funding through the Department of Energy (DOE), Office of Basic Energy Sciences, Division of Materials Sciences and Engineering, under Contract No. DE-AC02-76SF0051 (single-crystal synthesis). The EXAFS experiments were performed at the Stanford Synchrotron Radiation Lightsource (SSRL), which is supported by the U.S. Department of Energy, Office of Science, Office of Basic Energy Sciences, under Contract No. DE-AC02-76SF00515. Part of this work (SXRD) was performed at the Stanford Nano Shared Facilities, supported by the National Science Foundation under Award No. ECCS-2026822.

APPENDIX: EXPERIMENTAL DETAILS

1. X-ray-absorption data: samples and data collection

EXAFS samples are fabricated by grinding high-quality single crystals into fine powders to avoid the presence of single-crystal diffraction peaks that interfere with the EXAFS oscillations. The $CH_3NH_3PbBr_3$ samples used for EXAFS are prepared via acidolysis of N-methylformamide (NMF) with HBr in the presence of $PbBr_2$ [67]. More specifically, 1-M of $PbBr_2$ (99.999%) is dissolved in a 1:5.7 volume ratio of HBr:NMF (HBr, 48 wt % in H_2O, $\geq$ 99.99%; NMF, 99%) and allowed to evolve for 96 h at room temperature. A few millimeter-size crystals are then removed from the growth solution and quickly dried with an absorbing soft cloth to remove excess solvent present on the surface of the crystal. The growth is done under ambient conditions. After letting the crystals dry for at least 24 h in a desiccator, they are quickly moved to a solvent-free N_2 box for grinding with an agate mortar and pestle to a μm-size powder, which is then sealed under N_2 atmosphere.

Two samples are used in this study; sample 1 (S1) is prepared from one large single crystal, while sample 2 (S2) is prepared from two smaller single crystals grown in the same batch. Because of the elastic softness of the crystals, the possibility exists that grinding will introduce disorder and annealing is therefore considered. However, because of degradation concerns, a moderate annealing program of 15 min at 90°C is selected to reduce any disorder introduced by grinding. The annealed powders are spread onto tape using a fine brush to remove particles larger than 5 μm. Two pieces of tape are pressed together to make a double layer and three double layers are stacked to make the EXAFS samples.

The x-ray data were collected at the Stanford Synchrotron Radiation Lightsource (SSRL) on beamline 4–1 using a double monochromator with Si(220) crystals. An Oxford helium cryostat is used for temperatures from 5–300 K, together with a standard transmission setup using nitrogen gas ionization chambers for I_0 and I_1. The samples are oriented 60° to the x-ray beam to increase the path length, and the slit size is 0.4×6 mm^2; the beamline is detuned by 40% to reduce harmonics. The vertical slit size is chosen so that the monochromator energy resolution is well below the core-hole lifetime broadening energy.

The resulting step heights at the Pb L_{III} edge are 0.48 and 0.32 for samples S1 and S2, respectively; step heights at the Br K edge are about 40% higher. EXAFS data for annealed and unannealed samples are first compared at 10 K. The amplitudes for annealed samples are slightly larger and, subsequently, the full temperature-dependent study is carried out on the annealed samples; three scans are collected at 11 different temperatures for each. Analysis of S1, S2 yields similar results for all refined parameters. We indicate which sample data are plotted for each figure.

The Br K-edge EXAFS data are corrected to remove weak contributions from Pb L_{III} oscillations (Pb L_{III} edge, 13 055 eV; Br K edge, 13 474 eV). Details are provided in and Fig. S5 within the Supplementary Material [39].

The absorption data are reduced using the suite of programs, RSXAP [68], of which "reduce" incorporates standard techniques to remove the backgrounds, below and above the edge. After removing the pre-edge background, the edges are normalized just above the edge. The k range for the Pb L_{III}-edge data is limited by the Br K edge to about 10.3 Å^{-1}.

2. $MAPbBr_3$ crystallization and single-crystal x-ray diffraction

$CH_3NH_3PbBr_3$ crystals for SXRD are prepared by inverse temperature crystallization. A 1-M solution of $PbBr_2$ and CH_3NH_3Br in dimethylformamide is prepared and passed through a 0.22-μm filter; the filtered solution is heated to 82 °C in an oil bath and removed after 30 min. $CH_3NH_3PbBr_3$ crystals are isolated quickly

from the cooling mother liquor to avoid redissolution. Crystals are mounted on an x-ray transparent MiTeGen microloop using Paratone oil and single-crystal x-ray diffraction is performed on a Bruker D8 Venture diffractometer equipped with a Photon 100 CMOS detector. The temperature is varied from 100–300 K with an Oxford Cryostream.

Data are collected from ϕ and ω scans using Mo-Kα radiation ($\lambda = 0.710\,73$ Å). The frames are integrated using SAINT V8.38A and absorption correction is performed with SADABS-2016/2, both implemented in the Bruker APEX 3 software. Initial space group determination is performed with XPREP, with space group assignment based on reported structures, systematic absences, $|E * E - 1|$ statistics, and refinement statistics. The structure is solved using direct methods with the SHELXT software [69] and refined using a least-squares method implemented by SHELXL-2014/7 in the Olex 2 software package.

The Pb and Br thermal displacement parameters are refined anisotropically, whereas the C, N, and H parameters are refined isotropically. Because of the well-known dynamic cation disorder in the tetragonal and cubic phases, the methylammonium cation is confined to reside along high symmetry directions determined by residual electron densities. Additional constraints are applied to the C—N bond length (1.47 Å) and to fix fractional occupancy to maintain stoichiometry. The CIFs obtained from structural refinements are provided as Supplementary Material and have been deposited in the HybriD^3 database [70] with dataset IDs 2283, 2285–2296.

3. Correlated motion of Pb and Br

The correlated motions of neighboring atoms can be inferred from a comparison of the thermal parameters for individual atoms in diffraction with the mean-squared relative displacement (MSRD) parameter in EXAFS, σ^2, for a given pair of atoms, A and B. The MSRD σ^2 is then given by

$$\begin{aligned}\sigma^2 &= \langle(\delta R_A - \delta R_B)^2\rangle \\ &= \langle\delta R_A^2\rangle + \langle\delta R_B^2\rangle - 2\langle\delta R_A * \delta R_B\rangle,\end{aligned} \tag{A1}$$

where $\langle\cdot\rangle$ denotes a spatial average, δR_A and δR_B are displacements of the two atoms along the bond length, and $\langle\delta R_A^2\rangle = U_\parallel^A$, the ADP determined in diffraction. When the displacements are correlated, term $\langle\delta R_A * \delta R_B\rangle$ is not zero and σ^2 can be smaller or larger than $\langle\delta R_A^2\rangle + \langle\delta R_B^2\rangle$ depending on whether the displacements are in phase or out of phase. A correlation coefficient, ϕ, can be defined by [38] $\langle\delta R_A * \delta R_B\rangle = \phi * (\sqrt{\langle\delta R_A^2\rangle} * \sqrt{\langle\delta R_B^2\rangle})$. A similar equation to Eq. (A1) can also be defined for perpendicular motion, [36] but $\sigma_\perp^2$ is not directly measured in EXAFS.

Then the degrees of correlation, both parallel and perpendicular to the bond, are defined as [36–38]

$$\phi_\parallel = \frac{U_\parallel^A + U_\parallel^B - \sigma_\parallel^2}{2\sqrt{U_\parallel^A}\sqrt{U_\parallel^B}}, \tag{A2}$$

$$\phi_\perp = \frac{U_\perp^A + U_\perp^B - \sigma_\perp^2/2}{2\sqrt{U_\perp^A}\sqrt{U_\perp^B}}. \tag{A3}$$

These correlation coefficients range from $\phi = 1$ to $\phi = -1$, with the two limits representing completely correlated and anticorrelated motion, respectively. Here $\phi_\parallel$ is directly evaluated from Eq. (A2) using experimentally determined ADPs and EXAFS σ^2.

The perpendicular EXAFS $\sigma_\perp^2$ can be approximated from the EXAFS bond length r_{avg} and XRD bond length R_C using [36]

$$r_{\text{avg}} = R_C + \frac{\sigma_\perp^2}{2R_C}, \tag{A4}$$

where $\sigma^2 = \sigma_\parallel^2 = \sigma_\perp^2/2$ in the case of isotropic vibrations. The factor-of-2 difference between $\sigma_\parallel^2$ and $\sigma_\perp^2$ arises because $\sigma_\perp^2$ projects the perpendicular component within one plane only [36].

4. *Ab initio* molecular dynamics simulations

AIMD simulations are carried out using the FHI-aims all-electron electronic structure code [43]. The $MAPbBr_3$ structures are simulated in the orthorhombic, tetragonal, and cubic phases, using 96-atom unit cells (i.e., $2 \times 2 \times 2$ repetitions of the minimal stoichiometric unit of $MAPbBr_3$ in real space). Periodic images of the local bonding features of primary interest in this work are well separated from one another in this supercell geometry. Single-crystal XRD structures are used to provide initial atomic positions. These positions are then further relaxed to local minima of the Born-Oppenheimer potential energy surface while holding the lattice parameters constant, and the resulting relaxed structures are used as low-energy structures to initialize the AIMD simulations. The lattice parameters of the experimental input structures, as well as the fully optimized structure, are listed in Table S1 within the Supplementary Material [39]. The fully optimized structures, used as inputs for AIMD simulations, are shown in Supplementary Material Fig. S14.

The "intermediate" basis sets and numerical settings of FHI-aims are used together with the Perdew-Burke-Ernzerhof exchange correlation functional [44] and the Tkatchenko-Scheffler [45] dispersion correction scheme. The k-point grids are set to $4 \times 4 \times 4$. In past studies by some of us (e.g., Refs. [71–73]), this level of theory was shown to yield close agreement between experimentally

and computationally determined structures of complex hybrid perovskites. The frozen core approximation [74] was used to accelerate the AIMD simulations, freezing only very low-lying core orbitals below −900 eV. The accuracy of this method was thoroughly evaluated by Yu *et al.* [74], showing that the total energy error is practically negligible already when freezing all orbitals below $E = -200$ eV.

AIMD trajectories of five picoseconds in length within the constant-volume, constant-temperature (*NVT*) ensemble and with 0.75 fs timesteps are used to equilibrate the $MAPBr_3$ system at temperatures $T = 100$, 200, and 300 K, respectively. The Bussi-Donadio-Parrinello stochastic velocity rescaling thermostat [75] is used to regulate the temperature. At the outset of the *NVT* simulation, the Maxwell-Boltzmann distribution is used to initialize the atomic velocities corresponding to 600 K. Using the equilibrated atomic structure and velocities obtained from the *NVT* simulation, we then run additional AIMD simulations of 10–30 ps in length within the microcanonical constant-volume, constant-energy (*NVE*) ensemble using an integration time step of 0.75 fs. The structures derived from average atomic configurations of the *NVE* simulations are presented in Fig. S15 within the Supplementary Material [39].

The AIMD simulations at each temperature are analyzed to obtain the bond length, σ^2_{MD}, and C_3^{MD} for the nearest-neighbor Pb-Br pair distribution function. For direct comparison to experimental EXAFS and XRD results, the Pb—Br bond length is calculated in two different ways. First, the EXAFS-equivalent $r_{\mathrm{avg}}^{\mathrm{MD}}$ is calculated with the average Pb—Br bond length of each AIMD snapshot:

$$r_{\mathrm{avg}}^{\mathrm{MD}} = \frac{\sum_{i=1}^{G}\sum_{j=1}^{48} L_{ij}\,(\mathrm{Pb}-\mathrm{Br})}{G \times 48}. \tag{A5}$$

Here i denotes the structure at one AIMD snapshot, G is the total number of snapshot structures in the AIMD trajectory, j indexes the 48 Pb—Br bonds in one snapshot structure, and $L_{ij}\,(\mathrm{Pb}-\mathrm{Br})$ is the Pb—Br bond length. Second, the XRD-equivalent R_C^{MD} is alternatively calculated from the average AIMD atomic structure $\mathbf{U}$ generated from the entire AIMD trajectory:

$$\begin{aligned} \mathbf{U} &= \frac{\sum_{i=1}^{G}\mathbf{U}_i}{G}, \\ R_C^{\mathrm{MD}} &= \frac{\sum_{j=1}^{48} L_j\,(\mathrm{Pb}-\mathrm{Br})}{48}. \end{aligned} \tag{A6}$$

Here $\mathbf{U}_i$ is the atomic structure of one AIMD snapshot, j indexes the 48 Pb—Br bonds of $\mathbf{U}$, and $L_j\,(\mathrm{Pb—Br})$ denotes the distance between the center of the Pb distribution and the center of the Br distribution.

The anisotropic displacement parameter tensor U_{MD}^{A} for an atom A is calculated as mean-squared displacements:

$$\begin{aligned} U_{ii} &= \langle (x_i - \bar{x}_i)^2 \rangle, \\ U_{ij} &= \langle (x_i - \bar{x}_i)(x_j - \bar{x}_j) \rangle. \end{aligned} \tag{A7}$$

Here $i,j = 1,2,3$ and the x_i are the atomic position coordinates on the x, y, z Cartesian axis, and the $\bar{x}_i$ are the coordinates of the average position of atom A. The conversion to $U_{\parallel}^{\mathrm{MD}}$ and $U_{\perp}^{\mathrm{MD}}$ follows the procedure outlined in the Supplementary Material [39]. We calculate $\phi_{\perp}^{\mathrm{MD}}$ and $\phi_{\parallel}^{\mathrm{MD}}$ using Eqs. (A2)–(A4) with AIMD ADPs and bond lengths. A direct method for calculating $\sigma^2_{\perp,\mathrm{MD}}$ is presented in the Supplementary Material [Eq. (S7)], which yields similar results to Eq. (A4), as shown in Supplementary Material Table SII.

[1] H. Min, D. Y. Lee, J. Kim, G. Kim, K. S. Lee, J. Kim, M. J. Paik, Y. K. Kim, K. S. Kim, M. G. Kim, T. J. Shin, and S. Il Seok, Perovskite solar cells with atomically coherent interlayers on SnO_2 electrodes, Nature **598**, 444 (2021).

[2] R. Lin, J. Xu, M. Wei, Y. Wang, Z. Qin, Z. Liu, J. Wu, K. Xiao, B. Chen, S. M. Park, G. Chen, H. R. Atapattu, K. R. Graham, J. Xu, J. Zhu, L. Li, C. Zhang, E. H. Sargent, and H. Tan, All-perovskite tandem solar cells with improved grain surface passivation, Nature **603**, 73 (2022).

[3] D. A. Egger, A. Bera, D. Cahen, G. Hodes, T. Kirchartz, L. Kronik, R. Lovrincic, A. M. Rappe, D. R. Reichman, and O. Yaffe, What remains unexplained about the properties of halide perovskites?, Adv. Mater. **30**, 1800691 (2018).

[4] M. Z. Mayers, L. Z. Tan, D. A. Egger, A. M. Rappe, and D. R. Reichman, How lattice and charge fluctuations control carrier dynamics in halide perovskites, Nano Lett. **18**, 8041 (2018).

[5] J. M. Frost and A. Walsh, What is moving in hybrid halide perovskite solar cells?, Acc. Chem. Res. **49**, 528 (2016).

[6] C. Katan, A. D. Mohite, and J. Even, Entropy in halide perovskites, Nat. Mater. **17**, 377 (2018).

[7] M. Songvilay, Z. Wang, V. G. Sakai, T. Guidi, M. Bari, Z.-G. Ye, G. Xu, K. L. Brown, P. M. Gehring, and C. Stock, Decoupled molecular and inorganic framework dynamics in $CH_3NH_3PbCl_3$, Phys. Rev. Mater. **3**, 125406 (2019).

[8] I. P. Swainson, R. P. Hammond, C. Soullière, O. Knop, and W. Massa, Phase transitions in the perovskite methylammonium lead bromide, $CH_3ND_3PbBr_3$, J. Solid State Chem. **176**, 97 (2003).

[9] P. S. Whitfield, N. Herron, W. E. Guise, K. Page, Y. Q. Cheng, I. Milas, and M. K. Crawford, Structures, phase transitions and tricritical behavior of the hybrid perovskite methyl ammonium lead iodide, Sci. Rep. **6**, 35685 (2016).

[10] Y. Guo, O. Yaffe, T. D. Hull, J. S. Owen, D. R. Reichman, and L. E. Brus, Dynamic emission Stokes shift and liquid-like dielectric solvation of band edge carriers in lead-halide perovskites, Nat. Commun. **10**, 1 (2019).

[11] M. T. Weller, O. J. Weber, P. F. Henry, A. M. D. Pumpo, and T. C. Hansen, Complete structure and cation orientation in

the perovskite photovoltaic methylammonium lead iodide between 100 and 352 K, Chem. Commun. **51**, 4180 (2015).

[12] T. Chen, B. J. Foley, B. Ipek, M. Tyagi, J. R. D. Copley, C. M. Brown, J. J. Choi, and S.-H. Lee, Rotational dynamics of organic cations in the $CH_3NH_3PbI_3$ perovskite, Phys. Chem. Chem. Phys. **17**, 31278 (2015).

[13] Y. Guo, O. Yaffe, D. W. Paley, A. N. Beecher, T. D. Hull, G. Szpak, J. S. Owen, L. E. Brus, and M. A. Pimenta, Interplay between organic cations and inorganic framework and incommensurability in hybrid lead-halide perovskite $CH_3NH_3PbBr_3$, Phys. Rev. Mater. **1**, 042401 (2017).

[14] B. Yang, W. Ming, M.-H. Du, J. K. Keum, A. A. Puretzky, C. M. Rouleau, J. Huang, D. B. Geohegan, X. Wang, and K. Xiao, Real-time observation of order-disorder transformation of organic cations induced phase transition and anomalous photoluminescence in hybrid perovskites, Adv. Mater. **30**, 1705801 (2018).

[15] W.-H. Li, C.-H. Lee, T.-Y. Ling, M.-H. Ma, P.-C. Wei, J.-H. He, C.-M. Wu, J.-C. Peng, G. Xu, Y. Zhao, and J. W. Lynn, Dual lattice incommensurabilities and enhanced lattice perfection by low-temperature thermal annealing in photoelectric $CH_3NH_3PbBr_3$, Phys. Rev. Mater. **5**, 025401 (2021).

[16] D. Wiedemann, J. Breternitz, D. W. Paley, and S. Schorr, Hybrid perovskite at full tilt: Structure and symmetry relations of the incommensurately modulated phase of methylammonium lead bromide, $MAPbBr_3$, J. Phys. Chem. Lett. **12**, 2358 (2021).

[17] J. Jeong *et al.*, Pseudo-halide anion engineering for α-$FAPbI_3$ perovskite solar cells, Nature **592**, 381 (2021).

[18] J. H. Heo, D. H. Song, and S. H. Im, Planar $CH_3NH_3PbBr_3$ hybrid solar cells with 10.4% power conversion efficiency, fabricated by controlled crystallization in the spin-coating process, Adv. Mater. **26**, 8179 (2014).

[19] E. Edri, S. Kirmayer, D. Cahen, and G. Hodes, High open-circuit voltage solar cells based on organic–inorganic lead bromide perovskite, J. Phys. Chem. Lett. **4**, 897 (2013).

[20] S. Ryu, J. H. Noh, N. J. Jeon, Y. Chan Kim, W. S. Yang, J. Seo, and S. I. Seok, Voltage output of efficient perovskite solar cells with high open-circuit voltage and fill factor, Energy Environ. Sci. **7**, 2614 (2014).

[21] J. Huang, S. Xiang, J. Yu, and C.-Z. Li, Highly efficient prismatic perovskite solar cells, Energy Environ. Sci. **12**, 929 (2019).

[22] J. J. Yoo, G. Seo, M. R. Chua, T. G. Park, Y. Lu, F. Rotermund, Y.-K. Kim, C. S. Moon, N. J. Jeon, J.-P. Correa-Baena, V. Bulović, S. S. Shin, M. G. Bawendi, and J. Seo, Efficient perovskite solar cells via improved carrier management, Nature **590**, 587 (2021).

[23] X.-G. Zhao, G. M. Dalpian, Z. Wang, and A. Zunger, Polymorphous nature of cubic halide perovskites, Phys. Rev. B **101**, 155137 (2020).

[24] M. L. Holekevi Chandrappa, Z. Zhu, D. P. Fenning, and S. P. Ong, Correlated octahedral rotation and organic cation reorientation assist halide ion migration in lead halide perovskites, Chem. Mater. **33**, 4672 (2021).

[25] R. J. Worhatch, H. Kim, I. P. Swainson, A. L. Yonkeu, and S. J. L. Billinge, Study of local structure in selected organic–inorganic perovskites in the $Pm\bar{3}m$ phase, Chem. Mater. **20**, 1272 (2008).

[26] A. N. Beecher, O. E. Semonin, J. M. Skelton, J. M. Frost, M. W. Terban, H. Zhai, A. Alatas, J. S. Owen, A. Walsh, and S. J. L. Billinge, Direct observation of dynamic symmetry breaking above room temperature in methylammonium lead iodide perovskite, ACS Energy Lett. **1**, 880 (2016).

[27] G. Laurita, D. H. Fabini, C. C. Stoumpos, M. G. Kanatzidis, and R. Seshadri, Chemical tuning of dynamic cation off-centering in the cubic phases of hybrid tin and lead halide perovskites, Chem. Sci. **8**, 5628 (2017).

[28] J. Liu, A. E. Phillips, D. A. Keen, and M. T. Dove, Thermal disorder and bond anharmonicity in cesium lead iodide studied by neutron total scattering and the reverse Monte Carlo method, J. Phys. Chem. C **123**, 14934 (2019).

[29] N. J. Weadock, T. C. Sterling, J. A. Vigil, A. Gold-Parker, I. C. Smith, B. Ahammed, M. J. Krogstad, F. Ye, D. Voneshen, P. M. Gehring, A. M. Rappe, H.-G. Steinrück, E. Ertekin, H. I. Karunadasa, D. Reznik, and M. F. Toney, The nature of dynamic local order in $CH_3NH_3PbI_3$ and $CH_3NH_3PbBr_3$, Joule **7** (2023).

[30] H. Singh, R. Fei, Y. Rakita, M. Kulbak, D. Cahen, A. M. Rappe, and A. I. Frenkel, Origin of the anomalous Pb–Br bond dynamics in formamidinium lead bromide perovskites, Phys. Rev. B **101**, 054302 (2020).

[31] R. Comin, M. K. Crawford, A. H. Said, N. Herron, W. E. Guise, X. Wang, P. S. Whitfield, A. Jain, X. Gong, A. J. H. McGaughey, and E. H. Sargent, Lattice dynamics and the nature of structural transitions in organolead halide perovskites, Phys. Rev. B **94**, 094301 (2016).

[32] T. Lanigan-Atkins, X. He, M. J. Krogstad, D. M. Pajerowski, D. L. Abernathy, G. N. M. N. Xu, Z. Xu, D.-Y. Chung, M. G. Kanatzidis, S. Rosenkranz, R. Osborn, and O. Delaire, Two-dimensional overdamped fluctuations of the soft perovskite lattice in $CsPbBr_3$, Nat. Mater. **20**, 977 (2021).

[33] N. J. Weadock, P. M. Gehring, A. Gold-Parker, I. C. Smith, H. I. Karunadasa, and M. F. Toney, Test of the Dynamic-Domain and Critical Scattering Hypotheses in Cubic Methylammonium Lead Triiodide, Phys. Rev. Lett. **125**, 075701 (2020).

[34] G. Schuck, D. M. Többens, D. Wallacher, N. Grimm, T. S. Tien, and S. Schorr, Temperature-dependent EXAFS measurements of the Pb L3-edge allow quantification of the anharmonicity of the lead–halide bond of chlorine-substituted methylammonium (MA) lead triiodide, J. Phys. Chem. C **126**, 5388 (2022).

[35] J. M. Tranquada and R. Ingalls, Extended *x*-ray-absorption fine-structure study of anharmonicity in CuBr, Phys. Rev. B **28**, 3520 (1983).

[36] P. Fornasini and R. Grisenti, On EXAFS Debye-Waller factor and recent advances, J. Synchrotron. Radiat. **22**, 1242 (2015).

[37] C. H. Booth, F. Bridges, J. B. Boyce, T. Claeson, B. M. Lairson, R. Liang, and D. A. Bonn, Comparison of local structure measurements from c-axis polarized XAFS between a film and a single crystal of $YBa_2Cu_3O_{7-\delta}$ as a function of temperature, Phys. Rev. B **54**, 9542 (1996).

[38] C. H. Booth, F. Bridges, E. D. Bauer, G. G. Li, J. B. Boyce, T. Claeson, C. W. Chu, and Q. Xiong, XAFS measurements of negatively correlated atomic displacements in $HgBa_2CuO_{4+\delta}$, Phys. Rev. B **52**, R15745 (1995).

[39] See Supplemental Material at http://link.aps.org/supplemental/10.1103/PRXEnergy.2.033004 for crystallographic structure comparisons, ADP, and correlated motion derivations; additional EXAFS data, fitting descriptions, and literature comparisons; and a description and analysis of the MD calculations and results.

[40] C. A. López, M. V. Martínez-Huerta, M. C. Alvarez-Galván, P. Kayser, P. Gant, A. Castellanos-Gomez, M. T. Fernández-Díaz, F. Fauth, and J. A. Alonso, Elucidating the methylammonium (MA) conformation in $MAPbB_r3$ perovskite with application in solar cells, Inorg. Chem. **56**, 14214 (2017).

[41] K. Momma and F. Izumi, VESTA 3 for three-dimensional visualization of crystal, volumetric and morphology data, J. Appl. Crystallogr. **44**, 1272 (2011).

[42] F. Bridges, C. H. Booth, and G. G. Li, An iterative approach to atomic background removal in XAFS data analysis, Physica B **208&209**, 121 (1995).

[43] V. Blum, R. Gehrke, F. Hanke, P. Havu, V. Havu, X. Ren, K. Reuter, and M. Scheffler, Ab initio molecular simulations with numeric atom-centered orbitals, Comput. Phys. Commun. **180**, 2175 (2009).

[44] J. P. Perdew, K. Burke, and M. Ernzerhof, Generalized Gradient Approximation Made Simple, Phys. Rev. Lett. **77**, 3865 (1996).

[45] A. Tkatchenko and M. Scheffler, Accurate Molecular Van Der Waals Interactions from Ground-State Electron Density and Free-Atom Reference Data, Phys. Rev. Lett. **102**, 073005 (2009).

[46] R. T. Downs, Analysis of harmonic displacement factors, Rev. Mineral. Geochem. **41**, 61 (2000).

[47] G. Bunker, Application of the ratio method of EXAFS analysis to disordered systems, Nucl. Instrum. Methods **207**, 437 (1983).

[48] D. S. Yang, D. R. Fazzini, T. I. Morrison, L. Tröger, and G. Bunker, Modeling of pair distribution functions for XAFS in disordered systems, J. Non-Cryst. Solids **210**, 275 (1977).

[49] A. L. Ankudinov and J. J. Rehr, Relativistic calculations of spin-dependent x-ray-absorption spectra, Phys. Rev. B **56**, R1712 (1997).

[50] E. A. Stern, Number of relevant independent points in x-ray-absorption fine-structure spectra, Phys. Rev. B **48**, 9825 (1993).

[51] E. A. Stern, P. L̄ivņš, and Z. Zhang, Thermal vibration and melting from a local perspective, Phys. Rev. B **43**, 8850 (1991).

[52] A. I. Frenkel and J. J. Rehr, Thermal expansion and x-ray-absorption fine-structure cumulants, Phys. Rev. B **48**, 585 (1993).

[53] G. Dalba, P. Fornasini, R. Grisenti, and J. Purans, Sensitivity of Extended X-Ray-Absorption Fine Structure to Thermal Expansion, Phys. Rev. Lett. **82**, 4240 (1999).

[54] A. M. A. Leguy, J. M. Frost, A. P. McMahon, V. G. Sakai, W. Kockelmann, C. Law, X. Li, F. Foglia, A. Walsh, B. C. O'Regan, J. Nelson, J. T. Cabral, and P. R. F. Barnes, The dynamics of methylammonium ions in hybrid organic–inorganic perovskite solar cells, Nat. Commun. **6**, 7124 (2015).

[55] I. P. Swainson, C. Stock, S. F. Parker, L. Van Eijck, M. Russina, and J. W. Taylor, From soft harmonic phonons to fast relaxational dynamics in $CH_3NH_3PbBr_3$, Phys. Rev. B **92**, 100303 (2015).

[56] M. K. Jana, R. Song, H. Liu, D. R. Khanal, S. M. Janke, R. Zhao, C. Liu, Z. Valy Vardeny, V. Blum, and D. B. Mitzi, Organic-to-inorganic structural chirality transfer in a 2D hybrid perovskite and impact on Rashba-Dresselhaus spin-orbit coupling, Nat. Commun. **11**, 4699 (2020).

[57] T. Yin, Y. Fang, X. Fan, B. Zhang, J.-L. Kuo, T. J. White, G. M. Chow, J. Yan, and Z. X. Shen, Hydrogen-bonding evolution during the polymorphic transformations in $CH_3NH_3PbBr_3$: Experiment and theory, Chem. Mater. **29**, 5974 (2017).

[58] S. Zeiske, O. J. Sandberg, N. Zarrabi, C. M. Wolff, M. Raoufi, F. Peña-Camargo, E. Gutierrez-Partida, P. Meredith, M. Stolterfoht, and A. Armin, Static disorder in lead halide perovskites, J. Phys. Chem. Lett. **13**, 7280 (2022).

[59] D. Zhang, X. Hu, T. Chen, D. L. Abernathy, R. Kajimoto, M. Nakamura, M. Kofu, B. J. Foley, M. Yoon, J. J. Choi, and S.-H. Lee, Temporally decoherent and spatially coherent vibrations in metal halide perovskites, Phys. Rev. B **102**, 224310 (2020).

[60] G. Schuck, F. Lehmann, J. Ollivier, H. Mutka, and S. Schorr, Influence of chloride substitution on the rotational dynamics of methylammonium in $MAPbI_{3-x}Cl_x$ perovskites, J. Phys. Chem. C **123**, 11436 (2019).

[61] J. Endres, D. A. Egger, M. Kulbak, R. A. Kerner, L. Zhao, S. H. Silver, G. Hodes, B. P. Rand, D. Cahen, L. Kronik, and A. Kahn, Valence and conduction band densities of states of metal halide perovskites: A combined experimental–theoretical study, J. Phys. Chem. Lett. **7**, 2722 (2016).

[62] J. L. Knutson, J. D. Martin, and D. B. Mitzi, Tuning the band gap in hybrid tin iodide perovskite semiconductors using structural templating, Inorg. Chem. **44**, 4699 (2005).

[63] M. R. Filip, G. E. Eperon, H. J. Snaith, and F. Giustino, Steric engineering of metal-halide perovskites with tunable optical band gaps, Nat. Commun. **5**, 5757 (2014).

[64] T. S. Tien, N. Van Hung, N. T. Tuan, N. Van Nam, N. Q. An, N. T. Minh Thuy, V. T. Kim Lien, and N. Van Nghia, High-order EXAFS cumulants of diamond crystals based on a classical anharmonic correlated Einstein model, J. Phys. Chem. Solids **134**, 307 (2019).

[65] A. Glensk, B. Grabowski, T. Hickel, and J. Neugebauer, Understanding Anharmonicity in fcc Materials: From its Origin to *Ab Initio* Strategies beyond the Quasiharmonic Approximation, Phys. Rev. Lett. **114**, 195901 (2015).

[66] F. Bridges, B. Car, L. Sutton, M. Hoffman-Stapleton, T. Keiber, R. E. Baumbach, M. B. Maple, Z. Henkie, and R. Wawryk, Complex vibrations in arsenide skutterudites and oxyskutterudites, Phys. Rev. B **91**, 014109 (2015).

[67] J. Shamsi, A. L. Abdelhady, S. Accornero, M. Arciniegas, L. Goldoni, A. R. S. Kandada, A. Petrozza, and L. Manna, N-methylformamide as a source of methylammonium ions in the synthesis of lead halide perovskite nanocrystals and bulk crystals, ACS Energy Lett. **1**, 1042 (2016).

[68] C. H. Booth, *R-Space X-ray Absorption Package, 2010* (2010), http://lise.lbl.gov/RSXAP/.

[69] G. M. Sheldrick, SHELXT–Integrated space-group and crystal-structure determination, Acta Crystallogr., Sect. A: Found. Adv. **71**, 3 (2015).

[70] https://materials.hybrid3.duke.edu/.
[71] C. Liu, W. Huhn, K.-Z. Du, A. Vazquez-Mayagoitia, D. Dirkes, W. You, Y. Kanai, D. B. Mitzi, and V. Blum, Tunable Semiconductors: Control over Carrier States and Excitations in Layered Hybrid Organic-Inorganic Perovskites, Phys. Rev. Lett. **121**, 146401 (2018).
[72] M. K. Jana, C. Liu, S. Lidin, D. J. Dirkes, W. You, V. Blum, and D. B. Mitzi, Resolving rotational stacking disorder and electronic level alignment in a 2D oligothiophene-based lead iodide perovskite, Chem. Mater. **31**, 8523 (2019).
[73] N. E. Wright, X. Qin, J. Xu, L. L. Kelly, S. P. Harvey, M. F. Toney, V. Blum, and A. D. Stiff-Roberts, Influence of annealing and composition on the crystal structure of mixed-halide, Ruddlesden–Popper perovskites, Chem. Mater. **34**, 3109 (2022).
[74] V. W.-z. Yu, J. Moussa, and V. Blum, Accurate frozen core approximation for all-electron density-functional theory, J. Chem. Phys. **154**, 224107 (2021).
[75] G. Bussi, D. Donadio, and M. Parrinello, Canonical sampling through velocity rescaling, J. Chem. Phys. **126**, 014101 (2007).